中国光学（中英文） Chinese Optics 核心期刊

Phase distortion correction of fringe patterns in spaceborne Doppler asymmetric spatial heterodyne interferometry

PEI Hui-yi, JIANG Lun, WANG Jin-jiang, CUI Yong, FANG Yuan-xiang, ZHANG Jia-ming, CHEN Ci

Citation:
PEI Hui-yi, JIANG Lun, WANG Jin-jiang, CUI Yong, FANG Yuan-xiang, ZHANG Jia-ming, CHEN Ci. Phase distortion correction of fringe patterns in spaceborne Doppler asymmetric spatial heterodyne interferometry[J]. *Chinese Optics*, In press. doi: 10.37188/CO.EN-2024-0007
裴惠熠, 江伦, 王锦疆, 崔勇, 方远翔, 张家铭, 陈词. 星载多普勒非对称空间外差干涉测量中条纹图案的相位畸变校正[J]. 中国光学, 优先发表. doi: 10.37188/CO.EN-2024-0007

View online: https://doi.org/10.37188/CO.EN-2024-0007

Articles you may be interested in

Development of a doppler asymmetric spatial heterodyne interferometer for ground-based wind field detection at the 557.7 nm wavelength
557.7 nm波段地基探测风场的多普勒非对称空间外差干涉仪研制
Chinese Optics. 2023, 16(5): 1226 https://doi.org/10.37188/CO.EN-2022-0018

Multi-channel phase measurement system for the space laser interferometry
面向空间激光干涉的多通道相位测量系统
Chinese Optics. 2023, 16(5): 1089 https://doi.org/10.37188/CO.2022-0258

Phase measurement with dual-frequency grating in a nonlinear system
非线性系统中双频光栅相位测量
Chinese Optics. 2023, 16(3): 726 https://doi.org/10.37188/CO.EN.2022-0013

Dynamic 3D measurement error compensation technology based on phase-shifting and fringe projection
基于相移条纹投影的动态3D测量误差补偿技术
Chinese Optics. 2023, 16(1): 184 https://doi.org/10.37188/CO.EN.2022-0004

Panoramic bispectral infrared imaging interference spectrum measurement inversion instrument
全景双谱段红外成像干涉光谱测量反演仪器
Chinese Optics. 2022, 15(5): 1092 https://doi.org/10.37188/CO.2022-0114

Phase-extracting method of optical frequency scanning interference signals based on the CEEMD-HT algorithm
基于互补集合经验模态分解结合希尔伯特变换的光频扫描干涉信号相位提取方法
Chinese Optics. 2023, 16(3): 682 https://doi.org/10.37188/CO.2022-0173

文章编号　2097-1842(xxxx)x-0001-11

Phase distortion correction of fringe patterns in spaceborne Doppler asymmetric spatial heterodyne interferometry

PEI Hui-yi[1], JIANG Lun[1,2,3 *], WANG Jin-jiang[1], CUI Yong[1], FANG Yuan-xiang[1], ZHANG Jia-ming[1], CHEN Ci[4]

(1. *Changchun University of Science and Technology*, *School of Opto-Electronic Engineering*, *Changchun* 130022, *China*;
2. *Changchun University of Science and Technology*, *Key Laboratory of Fundamental Science for National Defense of Aero and Ground Laser Communication Technology*, *Changchun* 130022, *China*;
3. *Peng Cheng Laboratory*, *Shenzhen* 518000, *China*;
4. *Jilin Heng Hui Optoelectronics Technology Co.*, *Ltd*, *Changchun* 130022, *China*)

* *Corresponding author*, *E-mail*: *jlciomp*@163.*com*

Abstract: As an advanced technology for observing atmospheric winds, the spaceborne Doppler Asymmetric Spatial Heterodyne (DASH) interferometer also encounters challenges associated with phase distortion, particularly in limb sounding scenarios. This paper discusses interferogram modeling and phase distortion correction techniques for spaceborne DASH interferometers. The modeling of phase distortion interferograms with and without Doppler shift for limb observation was conducted, and the effectiveness of the analytical expression was verified through numerical simulation. The simulation results indicate that errors propagate layer by layer while using the onion-peeling inversion algorithm to handle phase-distorted interferograms. In contrast, the phase distortion correction algorithm can achieve effective correction. This phase correction method can be successfully applied to correct phase distortions in the interferograms of the spaceborne DASH interferometer, providing a feasible solution to enhance its measurement accuracy.

Key words: Doppler asymmetric spatial heterodyne spectroscopy; phase distortion; phase inversion; atmospheric wind measurement

收稿日期:2024-03-03; **修订日期**:2024-06-25

基金项目:吉林省科技发展计划项目(No. 20230201006GX)资助

Supported by Jilin Province Science and Technology Development Plan Project (No. 20230201006GX)

星载多普勒非对称空间外差干涉测量中条纹图案的相位畸变校正

裴惠熠[1], 江　伦[1,2,3*], 王锦疆[1], 崔　勇[1], 方远翔[1], 张家铭[1], 陈　词[4]
（1. 长春理工大学 光电工程学院, 吉林 长春 130012;
2. 长春理工大学 航空与地面激光通信技术国防基础科学重点实验室, 吉林 长春 130012;
3. 深圳鹏城实验室, 广东 深圳 518000;
4. 吉林珩辉光电科技有限公司, 吉林 长春 130012）

摘要: 作为观测大气风的先进技术, 星载多普勒非对称空间外差(DASH)干涉仪也面临着与相位畸变相关的挑战, 特别是在临边探测场景中。本文讨论了星载 DASH 干涉仪的干涉图建模和相位畸变校正技术。对临边观测中有与无多普勒频移的相位畸变干涉图进行了建模, 并通过数值模拟验证了解析表达式的有效性。仿真结果表明, 在使用洋葱皮反演算法处理相位失真干涉图时, 误差会逐层传播。相比之下, 相位畸变校正算法可以实现有效的校正。该相位校正方法可成功应用于星载 DASH 干涉仪干涉图中的相位畸变校正, 为提高其测量精度提供了可行的解决方案。

关　键　词: 多普勒非对称空间外差光谱; 相位畸变; 相位反演; 大气风测量
中图分类号: O482.31　　**文献标志码:** A　　**doi:** 10.37188/CO.EN-2024-0007　　**CSTR:** 32171.14.CO.EN-2024-0007

1 Introduction

The ionosphere constitutes a segment of Earth's atmosphere where gas molecules undergo ionization into plasma under the influence of solar radiation. Temperature changes produced by solar radiation lead to air pressure gradients that produce thermospheric winds[1-2]. Investigating thermospheric winds as an integral part of atmospheric models contributes to a more comprehensive understanding of dynamic atmospheric processes, including the influence of solar radiation on temperature, density, and pressure distribution. Such insights are crucial for researching climate and weather changes and predicting atmospheric behavior[3].

Passive optical techniques have been widely employed for detecting thermospheric wind and temperature over the past few decades[4]. The Fabry-Perot Interferometer (FPI) and Michelson Interferometer (MI) are representative passive optical technologies extensively used for detecting thermospheric winds and temperatures in satellite and ground applications[5]. FPI, while effective, imposes high manufacturing tolerances and has a limited field of view, often requiring large-sized systems to achieve high optical throughput[6]. On the other hand, traditional MI incorporates moving parts and is unsuitable for satellite-based observations. To address these challenges, the DASH concept was proposed in 2006[7]. The DASH interferometer can simultaneously detect multiple spectral lines without needing moving parts. Benefiting its structural advantages, the DASH interferometer maintains a relatively small device volume while implementing field-of-view expansion techniques[8]. Additionally, DASH interferometers can minimize instrument thermal drift by selecting suitable materials and geometric shapes, as well as additional instrument thermal drift tracking, making it suitable for satellite based observations[9].

The prerequisite for achieving high wind speed detection accuracy is a high-precision phase inversion algorithm. Spaceborne DASH interferometers commonly employ a two-dimensional detector array as the receiving device, projecting the atmosphere at different tangent heights onto various rows of the two-dimensional detector array to achieve

altitude profiling. While the phase of the fringes along each column of the two-dimensional detector array is theoretically identical, practical considerations such as the tilt or rotation of the grating, unevenness of the interferometer surface, non-uniformity of the interferometer glass index, or image distortion in the exit optics can introduce phase deviations, potentially impacting the accuracy of wind speed inversion[10].

Several studies have substantiated the feasibility of rectifying phase domain distortions in interferograms. Englert *et al*. introduced a method to ascertain frequency-dependent phase distortions, utilizing a tunable monochromatic light source to determine phase distortions as a function of wavenumber and optical path difference. The correction of phase distortions is accomplished by convolving the correction function in the spectral domain[11]. This approach was subsequently extended to DASH interferometers. A least squares algorithm was employed to fit linear functions to the phase curves of neon and oxygen lines, with the resulting residuals representing the instrument's phase distortion at these wavelengths[12]. The Michelson Interferometer for Global High-resolution Thermospheric Imaging (MIGHTI) instrument employs a method to correct fringe pattern phase distortions by measuring the phase of fringes during the TVAC (Thermal Vacuum Chamber) period under uniform diffuse emission line source illumination. The measured phase is then subtracted from a perfectly linear phase to obtain a phase distortion corrected image[13]. More recently, Wei *et al*. reported a method for correcting phase distortions in the phase domain by establishing a correction matrix. The results demonstrated that interferogram correction does not impact the retrieval of Doppler winds[14].

However, Limb sounding data from spaceborne DASH interferometers are typically processed using the onion-peeling inversion method, which has the disadvantage of propagating errors layer by layer. Phase distortions can result in errors that are more severe than those of ground-based DASH interferometers. This paper starts from theoretical derivation and extends the phase distortion correction method proposed by Wei *et al*.[14] for ground-based DASH interferometers to the correction of phase distortion in spaceborne DASH interferometers. Through theoretical analysis and numerical simulations to thoroughly analyze the process of distortion correction for spaceborne DASH interferometers.

2 Theoretical Analysis

The DASH interferometer improves upon the Michelson interferometer by substituting the mirrors at the ends of its two arms with diffraction gratings. In one of the arms, an additional optical path difference is introduced to augment the sensitivity of phase measurements. The principle diagram of the DASH interferometer is illustrated in Fig. 1. The incoming radiation undergoes division into two coherent wavefronts by a beam splitter. Subsequently, after reflection from diffraction gratings, these wavefronts reunite on the detector, creating a Fizeau fringe pattern. Unlike the Spatial Heterodyne Interferometer, where the zero optical path difference point is at the center of the detector, DASH shifts to a specific position on one side[8]. For a ground-based DASH interferometer, the interference pattern recorded at position x can be expressed as

$$I(x)=\int_0^{\infty} B(\sigma)\{1+\cos[2\pi(fx+2\sigma\Delta d)]\}d\sigma \quad , \tag{1}$$

where x represents the position along the horizontal axis of the detector, $B(\sigma)$ is the observed spectral density, σ is the central wavenumber of the emission line, Δd denotes the offset in one arm of the interferometer, and f signifies the spatial frequency. The spatial frequency can be calculated by

$$f=4\tan\theta_L(\sigma-\sigma_L) \quad , \tag{2}$$

where θ_L represents the Littrow angle, and σ_L is the Littrow wavenumber. The impact of neutral wind

manifests as a Doppler shift in the spectrum, $B(\sigma)$, which transforms into a phase shift in the interferogram $I(x)$ after modulation through the interferometer. Determining the Doppler velocity requires establishing the phase of the interferogram. This involves performing a Fourier transform on the interferogram, isolating the target spectrum through a window function, applying an inverse Fourier transform to the isolated spectrum to obtain a complex interferogram, and subsequently executing operations such as taking the ratio of the imaginary part to the real part, inverse tangent, and phase unwrapping to obtain the phase of the interferogram. To calculate the phase shift, it is essential to determine the phase difference between two interferograms—one with Doppler shift and one without Doppler shift. The relationship between the phase difference and the Doppler velocity is

$$\Delta\phi = \frac{2\pi D}{\lambda c} v \quad , \tag{3}$$

where $\Delta\phi$ is the phase shift, D is the optical path difference, v is the wind speed, λ is the rest wavelength of the emission line, and c is the speed of light.

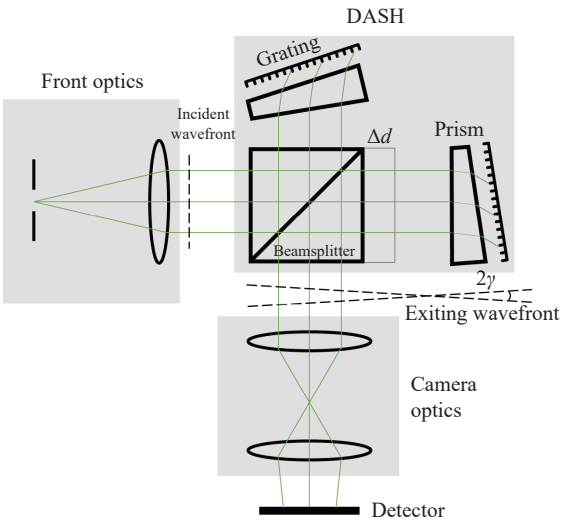

Fig. 1 Schematic diagram of DASH interferometer.

2.1 Line-of-sight Wind Retrieval

Eq. (1) delineates the interferogram expression derived from the ground-based DASH interferometer. However, within the Earth's atmosphere, each layer exhibits distinct wind, temperatures, and volume emission rates (VER). The spaceborne DASH interferometer operates in orbit at an altitude of approximately 500 km, employing limb sounding mode to observe the target atmospheric layer. Each pixel along a detector row is treated as a line of sight (LOS), encompassing contributions from various atmospheric layers. The limb-sounding configuration of the spaceborne DASH interferometer is depicted in Fig. 2, where n signifies the number of atmospheric layers, and m represents the LOS index. While the LOSs are tangent to their corresponding atmospheric layers, when m exceeds 0, the LOS intersects other layers before reaching the tangential point. These additional layers introduce extra Doppler shifts, rendering Eq. (1) unsuitable for describing the interferogram obtained by the spaceborne DASH interferometer. This equation is applicable only when the phase shift remains uniform for each row. Therefore, it becomes imperative to formulate a LOS integration model. Under the assumption of uniform wind, where airglow VER and wind speed are latitude and longitude independent but constant across small altitude layers, the signal received by the charge-coupled diode (CCD) in the mth row of the field of view is represented as $H_m(x)$[15]

$$H_m(x) = \sum_{n=0}^{N-1} \left(\int_0^{\infty} B_n(\sigma - \Delta\sigma_{mn}) \cdot (1 + \cos\{2\pi[f_n x + 2\sigma_n \Delta d]\}) d\sigma \right) w_{mn} \quad , \tag{4}$$

where N is the number of altitude layers, $B_n(\sigma)$ describes the unknown spectrum without Doppler shift at altitude n, $\Delta\sigma_{mn}$ represents the Doppler shift caused by LOS m at altitude n, and w_{mn} denotes the path length of the mth LOS through the nth layer. The expression is as follows

$$w_{mn} = 2\left(\sqrt{r_{n-1}^2 - r_n^2} - \sqrt{r_n^2 - r_m^2} \right) \quad , \tag{5}$$

Fig. 2 describes the physical meaning of Eq. (5), where the path length matrix w is defined

by the spacecraft's orbit, the vertical sampling resolution, and the LOS direction[16]. Here, r_n represents the altitude of the nth atmospheric layer plus the Earth's radius, and r_m is the altitude of the intersection point of the mth LOS plus the Earth's radius. After calibration steps, the corrected interferogram is presented as a complex interferogram. The Doppler shift $\Delta\sigma_{mn}$ in Eq. (4) is converted to phase shift $\Delta\phi_n$, and due to the angle between the LOS and the tangent to the layer, $\Delta\phi_n \cos\alpha_{mn}$ is used to represent the phase shift caused by wind within the nth layer in the LOS direction. $\cos\alpha_{mn}$ is expressed by the following formula

$$\cos\alpha_{mn} = \frac{r_m}{r_n}, m \geqslant n \quad , \tag{6}$$

The complex interferogram after calibration is represented as

$$H_m(x) = \sum_{n=0}^{m} I_n(x) e^{j\Delta\phi_n \cos\alpha_{mn}} w_{mn} \quad \forall m \in [0, M-1], \tag{7}$$

As the top measurement has no contributions from other altitudes, the attribute of the top altitude can be directly obtained from the measurement at the top. In the second measurement, contributions from the second and top layers are present. Therefore, the contribution of the top attribute can be removed from the second measurement, resulting in the attribute of the second layer. This process continues iteratively for subsequent measurements[15]. The inversion process can be expressed as follows

$$\begin{aligned} I_0(x) e^{j\Delta\phi_0} &= \frac{1}{w_{00}} H_0(x) \\ I_m(x) e^{j\Delta\phi_m} &= \frac{1}{w_{mm}} \left(H_m(x) - \sum_{n=0}^{m-1} I_n(x) e^{j\Delta\phi_n \cos\alpha_{mn}} w_{mn} \right) \\ \forall m \in [1, M-1] \quad , \end{aligned} \tag{8}$$

After performing the computation outlined in Eq. (8), the data following the onion peeling process is obtained. Each data row encompasses the phase shift induced by the wind within each layer along the LOS direction. Subsequently, utilizing the aforementioned wind retrieval method, corresponding phase values can be acquired and employed to calculate wind speed.

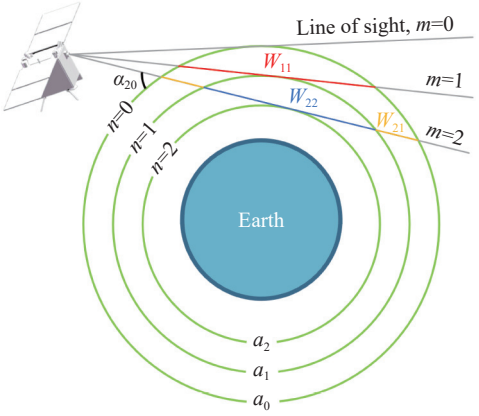

Fig. 2 Schematic diagram of limb sounding for spaceborne DASH interferometer. The angle between the tangent of the intersection of the mth LOS and the nth layer is α_{mn}.

2.2 Phase Distortion Modeling

Eq. (4) describes the fringe pattern obtained by the spaceborne DASH interferometer in an ideal state. As mentioned earlier, the fringe pattern obtained by the interferometer is not ideal; it is accompanied by the tilting and bending of the fringes. The tilt of the fringes is primarily caused by the tilted installation of the grating, resulting in a wavefront tilting in y direction and introducing an additional spatial modulation in y direction. According to the reports by Harlander *et al*. and Wei *et al*.[14, 17], the spatial frequency generated in y direction can be obtained by

$$f_y = 2\beta_1\sigma + \beta_2 m_g d^{-1} \quad , \tag{9}$$

where β_1 denotes a small angle of rotation of the grating about an axis perpendicular to the direction of the groove, and β_2 denotes a small angle of rotation of the grating about a line normal to the plane of the grating, m is the diffraction order, and d is the grating's groove spacing. The tilt of the grating leads to an additional spatial frequency, which can be divided into two parts: $2\beta_1\sigma$ is related to the incident wavenumber, and $\beta_2 m_g d^{-1}$ is associated with the diffraction order of the grating. Taking into ac-

count the tilt of the fringes and other phase distortion terms Θ, Eq. (7) is rewritten as

$$H_m(x,y)=\sum_{n=0}^{m} I_n(x)\cdot e^{j\Delta\phi_n\cos\alpha_{mn}+\left(2\beta_1\sigma+\beta_2 m_g d^{-1}\right)y+\Theta(\sigma,x,y)} w_{mn} \quad \forall m\in[0,M-1] \quad , \tag{10}$$

Merging several adjacent pixels on a sensor into a single pixel, known as pixel binning, represents a crucial technique for enhancing the signal-to-noise ratio of interference patterns, albeit at the cost of a reduction in resolution. Directly applying pixel binning to interference patterns with phase distortions results in a loss of contrast. The thermal effects within interferometers manifest as a universally encountered phenomenon, with specific instrument parameters, such as optical path difference and the refractive index of the field-widening prism, undergoing gradual changes over time. To correct the thermal drift of interferometers over time, the commonly employed method for quantifying interferometer thermal drift involves the utilization of an onboard calibration lamp as a reference source[18]. This method entails measuring the phase shift closely matching the wavelength of the airglow lines. By subtracting the phase of the calibration lines from that of the atmospheric fringes, the purpose of correcting the interferometer thermal drift is achieved. The wavelength of the calibration lamp differs from that of the airglow by approximately 0.1%[18]. Theoretically, phase distortions, as a systematic error, can also be approximately eliminated during this subtraction process. However, phase distortions are highly sensitive to minor variations in refractive index or optical component dimensions, resulting in a time-dependent and long-term variation in the phase response. Moreover, thermal changes exhibit periodicity related to the satellite's orbital altitude. Notably, not every instrument exposure allows for the simultaneous acquisition of interference patterns from the airglow and the calibration lamp. Inconsistent acquisition times, leads to additional errors during the correction process of phase distortions. Therefore, it is essential to develop a method for correcting phase distortions that can be applied during each exposure.

2.3 Phase Distortion Correction

As articulated in Eq. (10), distortion terms $2\beta_1\sigma+\beta_2 m_g d^{-1}$ and $\Theta(\sigma,x,y)$ manifest in the phase domain. A viable approach to mitigate these distortions involves conducting corrections in the phase domain, thus eliminating these distortion terms. The methodology for acquiring Doppler shifts in spaceborne DASH interferometers is akin to ground-based DASH interferometers. It necessitates two interferograms: one representing the Doppler shift induced by LOS wind and the other serving as a reference interferogram without any Doppler shift, commonly called the zero-wind interferogram. During the device's on-orbit operation, acquiring the interferogram of zero wind is impossible. Therefore, a "zero-wind maneuver" method is employed to obtain the interferogram of zero wind generated by airglow. The spacecraft performs yaw maneuvers, observing the same region of the atmosphere from opposite directions within a short time frame. Assuming the wind field remains relatively unchanged during this period, the obtained interferograms are inverted separately. Two wind profiles are derived from these inverted interferograms, and their summation should approximate zero, allowing the determination of the zero-wind phase[15]. Hence, it is imperative to correct two interferograms simultaneously. The expressions for interferograms, encompassing phase distortions, are provided for both non-Doppler-shifted and Doppler-shifted cases

$$H_m^{0,v}(x,y)=\sum_{n=0}^{m} B_n(\sigma_{0,v_n})\left(1+\cos\left\{2\pi[f_{0,v_n}(\sigma_{0,v_n})x+2\sigma_{0,v}\Delta d+\left(2\beta_1\sigma_{0,v_n}+\beta_2 m_g d^{-1}\right)y+\Theta(\sigma_{0,v_n},x,y)]\right\}\right)w_{mn}$$
$$\forall m\in[0,M-1] \quad , \tag{11}$$

Variations in incident wavenumber have induced changes in the terms related to wavenumber

in the interferogram phase. Interferograms with distinct incident wavenumbers will manifest varying spatial frequencies. Here, $2\sigma\Delta d$ signifies the phase extension arising from the bias of one arm of the DASH interferometer, intending to increase the numerical value of the phase and, consequently, enhance the precision of wind speed measurements. $\Theta(\sigma,x,y)$ denotes the phase distortion, exhibiting variations with changes in the incident wavenumber σ and CCD positions (x and y). Post-Fourier transformation of the interferogram, non-zero values are present around the two exponential functions corresponding to $+f$ and $-f$. By applying a suitable window function to segregate $+f$, the modulated component of the interferogram is obtained following the inverse Fourier transformation. Ultimately, operations involving the imaginary part to real part ratio, inverse tangent, and unwrapping are conducted on the complex interferograms to extract the interferogram's phase. The LOS of the satellite-borne DASH interferometer may encompass contributions from numerous layers, including multiple layers of contributions in the phase. For simplicity in the analysis process, the phase of the non-Doppler shift fringes and the phase of the mth row fringes with Doppler shift are represented as $\phi_{0,m}$ before performing the "onion-peeling"

$$\phi_{0,m} = 2\pi\cdot\left[f_{0,m}x + 2\sigma_{0,m}\Delta d + \left(2\beta_1\sigma_{0,m} + \beta_2 m_g d^{-1}\right)y + \Theta_{0,m}\right], \quad (12)$$

The spatial frequency of an interferogram without Doppler shift is identified as f_0. For a given incident wavenumber, the spatial frequency of the generated interferogram can be determined using Eq. (2). The distortions in the phase of an interferogram without Doppler shift can be described as

$$\phi_0 - 2\pi f_0 x = 2\pi\cdot\left[2\sigma_0 d + \left(2\beta_1\sigma_0 + \beta_2 m_g d^{-1}\right)y + \Theta_0\right], \quad (13)$$

The modulated component of the interferogram takes the form of an exponential function, incorporating distortion terms. Consequently, a correction matrix C is defined here

$$C = e^{-j2\pi\left[2\sigma_0\Delta d + \left(2\beta_1\sigma_0 + \beta_2 m_g d^{-1}\right)y + \Theta_0\right]} \quad (14)$$

Finally, the modulated component of the distorted interferogram is multiplied by the correction matrix C to obtain the corrected interferogram. The flowchart of phase distortion correction is shown in the Fig. 3. It is essential to note that both interferograms, with and without Doppler shift, require the utilization of the correction matrix generated from the zero-wind interferogram's phase. Following the correction for phase distortion, the phase of the interferogram with Doppler shift is expressed as

$$\phi_m = 2\pi\cdot\left[f_m x + 2(\sigma_m - \sigma_0)\Delta d + 2\beta_1(\sigma_m - \sigma_0)y + \Theta_m - \Theta_0\right], \quad (15)$$

Notably, the correction algorithm eliminates distortion terms from the phase for the zero-wind interferogram. However, the phase distortion terms are not entirely removed for interferograms with Doppler shift, and distortion terms $2\beta_1(\sigma_m - \sigma_0)y$ and $\Theta_m - \Theta_0$ persist. The grating and the interferometer connect through bonding, employing an adhesive with an extended curing time and low stress. Simultaneously, real-time monitoring of the interferogram is conducted during the adhesive curing process. The grating's tilt angle β_1 is meticulously adjusted to keep the interference fringes as vertical as possible, effectively suppressing undesired tilt. Hence, the tilt angle β_1 of the grating can be well-managed. The dependency of phase distortion term Θ on the wavenumber σ can be considered negligible. Simultaneously, the phase difference between the corrected interferogram with Doppler shift and the zero-wind interferogram is computed. This phase difference retains the phase extension introduced by the bias term Δd. Additionally, the corrected interferogram continues to encompass contributions from multiple atmospheric layers along a CCD row, this characteristic allows for the regular application of onion peeling for the inversion of the interferogram.

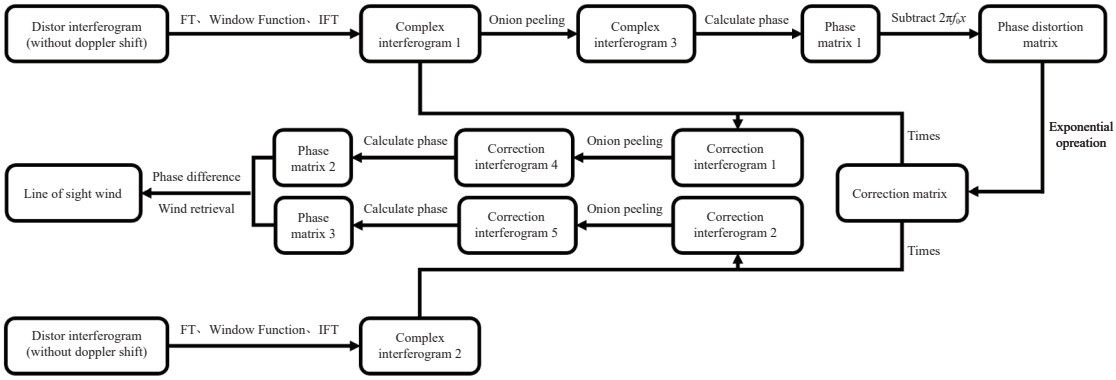

Fig. 3 The flowchart of phase distortion correction.

3 Simulated Phase Distortion Correction and Wind Retrieval

In the preceding section, we introduced an algorithm for correcting phase distortion in limb observation interferograms obtained from a spaceborne DASH interferometer. In this section, we present an illustrative example of forward simulation interferograms using incident light with a wavelength of 557.7 nm. The emphasis is on validating the effectiveness of phase distortion correction.

The interferometer parameters are outlined in Tab. 1, and the simulated interferogram is depicted in Fig. 4. A spherical symmetry assumption is applied to simplify the analysis, presuming that atmospheric parameters at each altitude layer are independent of latitude and longitude[16]. Simultaneously, to validate the impact of the phase distortion correction algorithm on wind speed retrieval, a simulated wind speed profile was input, and two interferograms with and without Doppler frequency shift were generated. No additional noise is introduced in the simulation. Initially, the inversion is performed directly on the uncorrected image, Fig. 5(a) presents the retrieved LOS wind profiles. The data in the figure indicates that the error gradually increases as the altitude decreases. This result validates the influence of phase distortion on the inversion process. Additionally, employing the onion-peeling method for interferogram inversion results in a cumulative layer-by-layer error accumulation during peeling. This accumulation is more pronounced than ground-based DASH interferometers, where the phase of each fringe in the interferogram remains consistent across every row.

Tab. 1 Parameters for simulation.

Parameters	Values
Wavelengths	557.7 nm
Littrow wavelengths	557.137 nm
OPD offset	20.363 mm
Detector resolution	82×1 024
Grating groove density	600 grooves/mm
Diffraction order	1
Pixel pitch	13 μm

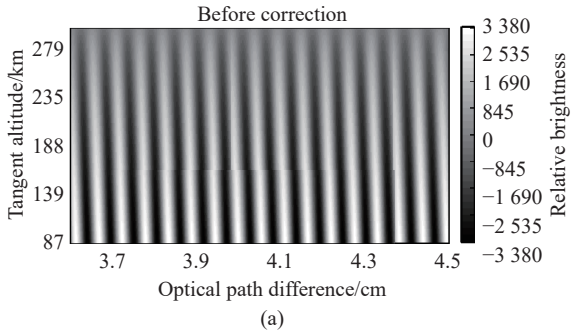

(a)

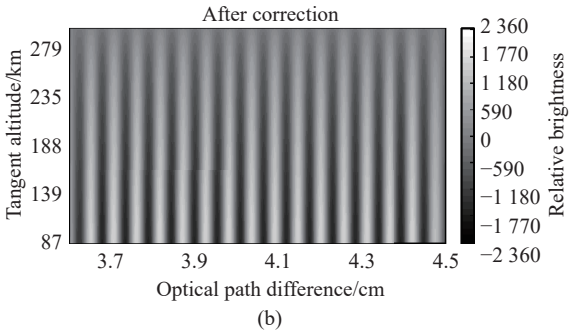

(b)

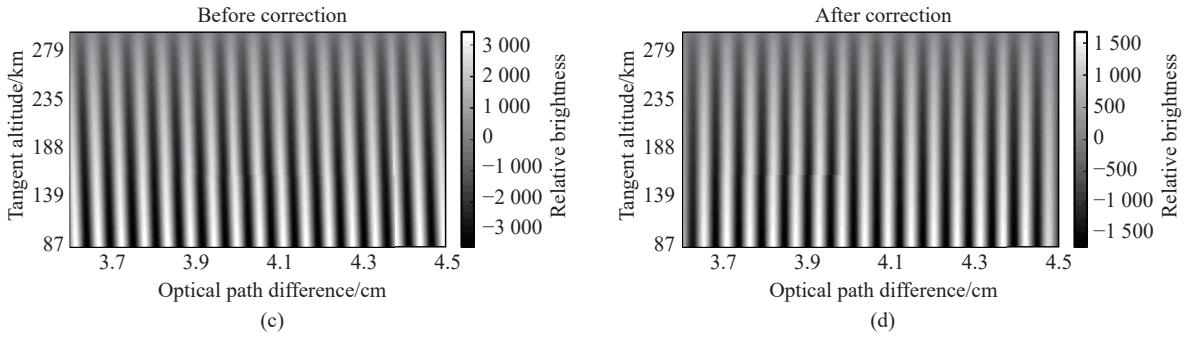

Fig. 4 Panel (a) shows a simulated non Doppler shift tilted fringe interferogram, panel (b) is the correction for panel (a), Panel (c) shows a simulated Doppler shift tilted fringe interferogram, panel (d) is the correction for panel (c). The vertical axis denotes the tangent altitude, and the horizontal axis represents the optical path difference. The simulated images have been vertically stretched, with the actual image proportions being 82×1024.

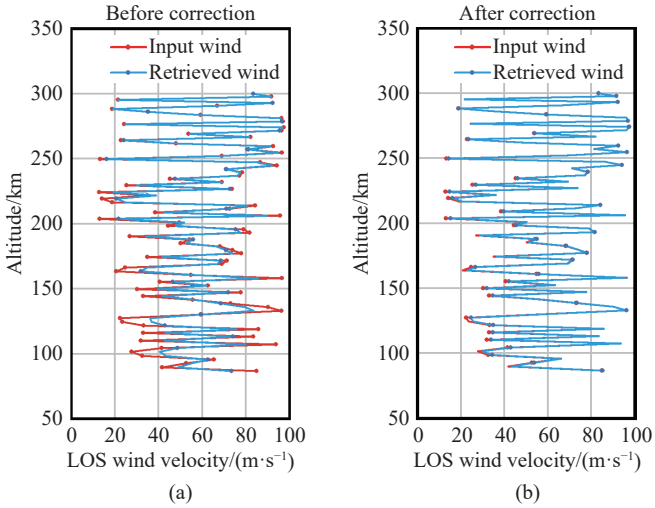

Fig. 5 Comparison between input wind profile and retrieved wind profile. The red line represents the input wind profile, while the blue line represents the retrieved wind profile. Panel (a) shows the data before phase distortion correction, and panel (b) shows the data after phase distortion correction.

Fig. 4(b) and (d) show the interferograms after phase distortion correction. The interference fringes exhibit no tilted features after correction. Fig. 5(b) showcases the retrieved LOS wind profiles using the corrected interferogram. The inverted profiles closely mirror the input wind profile, and the error in LOS wind diminishes with increasing altitude. This underscores the effectiveness of the phase distortion correction algorithm for rectifying interferograms produced by a spaceborne DASH interferometer in limb observation mode.

From previous theoretical derivations, it is known that even after phase distortion correction, a phase distortion term $2\beta_1(\sigma_m - \sigma_0)y$ remains in the interferogram, which may impact the accuracy of the inversion results. To analyze the impact of the residual phase distortion term, we simulated the phase changes caused by the residual phase distortion term in different rows of the detector based on the model parameters designed in Tab. 1. The detector employed 4×1 pixel binning in the y-direction, with an input wind speed of 100 m/s. The angle β_1 varied from -1 rad to 1 rad. The phase changes caused by the residual phase distortion term are shown in Fig. 6. When the angle β_1 rotates by 1 rad, the phase change in the 41 row of the detector is approximately 2.5×10^{-3} rad, equivalent to a wind speed error of 1.67 m/s. In practice, the angle β_1 can be controlled within a range of 100 μrad. Within this deflection range, the maximum phase change is

2.5×10^{-8} rad, corresponding to a wind speed error of 1.67×10^{-5} m/s. Considering the cumulative error characteristic of the onion peeling method in simulations, when the angle β_1 deflects by 100 μrad, the maximum wind speed retrieval error after phase distortion correction is 1.6 m/s, with an average relative error of 1.72%.

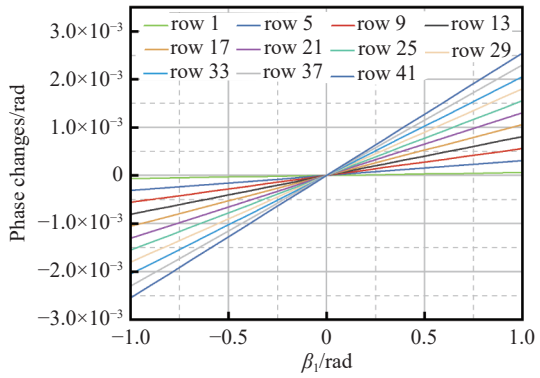

Fig. 6 After phase distortion correction, the phase changes caused by different angles β_1 in the residual phase distortion terms across different detector rows.

4 Conclusion

This paper delves into the intricacies of phase distortion correction in DASH interferometer, specifically in limb sounding scenarios for atmospheric wind field observations. One of the causes of phase distortion in the DASH interferometer is the deflection of the grating, which generates an additional modulation component in the y-direction. Phase distortion in the spaceborne DASH interferometer leads to cumulative errors layer by layer, resulting in a more severe impact compared to the ground-based DASH interferometer. Building on the existing phase distortion modeling of ground-based DASH interferometers, we extended this method to spaceborne DASH interferometers. We conducted simulations involving the modeling and correction of phase-distorted limb observation interferograms. In theoretical analysis, although residual phase distortion remains after correction, its impact on the inversion results is minimal. In simulations, a 100 μrad deviation in angle β_1 resulted in a residual phase distortion causing a wind speed error of 1.67×10^{-5} m/s. Simulation results demonstrate that the phase distortion correction method can be effectively applied to the spaceborne DASH interferometer.

References:

[1] GIRAUD A, PETIT M. *Ionospheric Techniques and Phenomena*[M]. Dordrecht: Springer, 1978. **(查阅网上资料, 请确认年份信息)**.

[2] VADAS S L, LIU H L. Generation of large-scale gravity waves and neutral winds in the thermosphere from the dissipation of convectively generated gravity waves[J]. *Journal of Geophysical Research: Space Physics*, 2009, 114(A10): A10310.

[3] WANG W B, BURNS A G, LIU J. Upper thermospheric winds: forcing, variability, and effects[M]//WANG W B, ZHANG Y L, PAXTON L J. Upper Atmosphere Dynamics and Energetics. Hoboken: American Geophysical Union, 2021: 41-63.

[4] MERIWETHER J W. Studies of thermospheric dynamics with a Fabry–Perot interferometer network: a review[J]. *Journal of Atmospheric and Solar-Terrestrial Physics*, 2006, 68(13): 1576-1589.

[5] MAKELA J J, BAUGHMAN M, NAVARRO L A, *et al*.. Validation of ICON-MIGHTI thermospheric wind observations: 1. Nighttime red-line ground-based fabry-perot interferometers[J]. *Journal of Geophysical Research: Space Physics*, 2021, 126(2): e2020JA028726.

[6] WEI D K. *Development of an optical instrument for the observation of neutral winds in Earth's upper atmosphere*[D]. Wuppertal: Bergische Universität, 2020.

[7] ENGLERT C R, HARLANDER J M, BABCOCK D D, *et al*.. Doppler asymmetric spatial heterodyne spectroscopy (DASH): an innovative concept for measuring winds in planetary atmospheres[J]. *Proceedings of SPIE*, 2006, 6303: 63030T.

[8] ENGLERT C R, BABCOCK D D, HARLANDER J M. Doppler asymmetric spatial heterodyne spectroscopy (DASH):

concept and experimental demonstration[J]. *Applied Optics*, 2007, 46(29): 7297-7307.

[9] WEI D K, ZHU Y J, LIU J L, *et al*.. Thermally stable monolithic Doppler asymmetric spatial heterodyne interferometer: optical design and laboratory performance[J]. *Optics Express*, 2020, 28(14): 19887-19900.

[10] ENGLERT C R, HARLANDER J M, MARR K D, *et al*.. Michelson interferometer for global high-resolution thermospheric imaging (MIGHTI) on-orbit wind observations: data analysis and instrument performance[J]. *Space Science Reviews*, 2023, 219(3): 27.

[11] ENGLERT C R, HARLANDER J M, CARDON J G, *et al*.. Correction of phase distortion in spatial heterodyne spectroscopy[J]. *Applied Optics*, 2004, 43(36): 6680-6687.

[12] ENGLERT C R, HARLANDER J M, EMMERT J T, *et al*.. Initial ground-based thermospheric wind measurements using Doppler asymmetric spatial heterodyne spectroscopy (DASH)[J]. *Optics Express*, 2010, 18(26): 27416-27430.

[13] HARLANDER J M, ENGLERT C R, MARR K D, *et al*.. On the uncertainties in determining fringe phase in Doppler asymmetric spatial heterodyne spectroscopy[J]. *Applied Optics*, 2019, 58(13): 3613-3619.

[14] WEI D K, GONG Q CH, CHEN Q Y, *et al*.. Modeling and correction of fringe patterns in Doppler asymmetric spatial heterodyne interferometry[J]. *Applied Optics*, 2022, 61(35): 10528-10537.

[15] HARDING B J, MAKELA J J, ENGLERT C R, *et al*.. The MIGHTI wind retrieval algorithm: description and verification[J]. *Space Science Reviews*, 2017, 212(1): 585-600.

[16] WU Y J J, HARDING B J, TRIPLETT C C, *et al*.. Errors from asymmetric emission rate in spaceborne, limb sounding doppler interferometry: a correction algorithm with application to ICON/MIGHTI[J]. *Earth and Space Science*, 2020, 7(10): e2020EA001164.

[17] HARLANDER J, REYNOLDS R J, ROESLER F L. Spatial heterodyne spectroscopy for the exploration of diffuse interstellar emission lines at far-ultraviolet wavelengths[J]. *The Astrophysical Journal*, 1992, 396(2): 730-740.

[18] ENGLERT C R, HARLANDER J M, BROWN C M, *et al*.. Michelson Interferometer for Global High-Resolution Thermospheric Imaging (MIGHTI): instrument design and calibration[J]. *Space Science Reviews*, 2017, 212(1-2): 553-584.

Author Biographics:

JIANG Lun (1984—), male, from Huang-gang, Hubei Province, Ph.D, researcher/doctoral supervisor, obtained his Ph.D from Changchun Institute of Optics, Fine Mechanics and Physics, Chinese Academy of Sciences in 2012, mainly engaged in optical system design, space optics and space optical communication technology research. E-mail: jlciomp@163.com